


Aerodynamics and stability of hawkmoth forward flight with flexible wing hinge

Yujing Xue, Xuefei Cai, and Hao Liu ^{*}

Shanghai Jiao Tong University and Chiba University International Cooperative Research Center (SJTU-CU ICRC), Shanghai Jiao Tong University, 800 Dongchuan Road, Minhang District, Shanghai 200240, People's Republic of China
and Graduate School of Engineering, Chiba University 1-33, Yayoi-cho, Inage-ku, Chiba 263-8522, Japan



(Received 22 January 2024; accepted 21 May 2024; published 11 June 2024)

Flying insects can achieve remarkable and robust flapping aerodynamic performance and flight stability in various environments partially owing to the passive mechanisms of their wings and bodies, but a careful analysis associated with flexible wing hinge for forward flight is missing. Here we develop a fluid-structure interaction model that couples the one-torsional-spring-based elastic wing-hinge dynamics with the flapping aerodynamics to study the aerodynamics and flight stability of the hawkmoth, *Manduca sexta*, with flexible wing hinge at various flight velocities. The results show that the leading-edge vortex, the body vortex, and their interactions are responsible for augmenting the vertical force production interactively at all flight velocities, enabling a 6.5% increase at fast flight speeds. The elastic storage enabled by the flexible wing hinge exhibits a *J* curve, achieving high power efficiency at intermediate forward flight velocities. We verify that the realistic wing-hinge stiffness leads to optimal aerodynamic performance in terms of vertical force production and power cost. External disturbance rejection based on the flexible wing hinge is highly robust in multiple directions, independent of the forward flight velocity. This study highlights the importance and significance of flexible wing hinges in biomimetic designs for flapping micro aerial vehicles.

DOI: [10.1103/PhysRevFluids.9.063101](https://doi.org/10.1103/PhysRevFluids.9.063101)

I. INTRODUCTION

Flying insects with flapping wings are capable of achieving remarkable unsteady aerodynamic performance and robust maneuverability in complex natural environments [1]. They utilize their intrinsic musculoskeletal system in terms of the deformable body, flexible wings, and wing hinges [2–6], which work interactively and complementarily to enable robust aerodynamic performance and flight stability in hovering and forward flight. The asynchronous indirect muscles on the thorax [7] and the synchronous direct steering muscles within the wing hinge [8] are used to control the flapping wing motion, while the musculoskeletal system drives the wing in a passive way [9] via the flexible wing hinge through the interplay between the inertial, aerodynamic, and elastic restoring forces, thus altering the wing kinematics and aerodynamics [10]. How these flexible wing hinges alter the unsteady aerodynamics while retaining robustness at various forward flight velocities remains an open question.

The flapping aerodynamics of an insectlike wing-body model undergoing flapping flight have been studied using rigid wing-hinge models. The rigid wing-body interaction of the leading-edge

^{*}Contact author: hliu@faculty.chiba-u.jp

vortex (LEV) and body vortex (BV) in the vicinity of the wing root has been investigated experimentally [11–13] and computationally [14–22] for the hovering and forward flight of insects and birds. Several computational fluid-dynamics (CFD)-based studies on the flapping flight of cicadas [14,15], fruit flies [18], hawkmoths [17], and hummingbirds [16,19] have confirmed the formation of body-based vortices attached to the upper body surface. Additionally, high lift enhancements owing to rigid wing-body interaction have been identified in the hovering flight of fruit flies [20–22] and in the forward flight of cicadas [14,15] and hummingbirds [16,19]. Recent studies on the forward flight of hawkmoths [23] also proved the crucial role of rigid wing-body interaction in aerodynamic performance, producing notable vertical force enhancements and energy saving over a broad range of flight velocities. However, the effects of wing-body interaction on the flapping aerodynamics and energetics in the case of flexible wing hinges remain poorly understood.

Recent studies on flapping aerodynamics with flexible wing hinges have focused on hovering flight. A strongly coupled fluid-structure interaction (FSI) method [24] was developed to explore the interaction between passive wing-pitch rotation and flapping aerodynamics, revealing that an advanced pitch up of the wing induced by a flexible feathering hinge [24] can enhance the lift force production via wake capture [25]. With consideration of the weak coupling between aerodynamics and a damped torsional spring, Beatus and Cohen [26] found that sufficient lift for the insect to stay airborne could be produced at a realistic power cost [27] through the passive and indirect alteration of the wing-pitch kinematics. Ishihara [28] introduced a two-torsional-spring model to combine the passive elevation and feathering motions, and reported a pronounced increase in vertical force under a figure-of-eight mode of the wing-tip path, which can be attributed to an intense LEV enhanced by passive upward elevation motion. Cai *et al.* [10] developed a FSI model to deal with the three-torsional-spring-based elastic wing-hinge dynamics in bumblebee hovering, proposing a strategy combining an active-controlled stroke with a passive-controlled wing pitch and deviation to enable optimal elastic storage. Furthermore, the flexible wing hinge enables robust flapping wing dynamics in terms of elastic storage, enabling high power efficiency to be achieved over a broad range of wing-hinge stiffnesses [10]. While recent advances have addressed some elastic wing-hinge-based mechanisms concerning insect hovering flight [29,30], a careful analysis of how the flexible wing-body interaction associated with elastic wing hinges alters the unsteady aerodynamics, energetics, and flight stability in forward flight is missing.

In this paper, we aim to identify how the elastic wing hinges associated with flexible wing-body interactions alter the unsteady aerodynamic performance while retaining robustness in the forward flight of the hawkmoth, *Manduca sexta*, over a broad range of flight velocities. In Sec. II, we describe a wing-body morphological model and realistic wing-body kinematics comprising hovering and five forward flight velocities, which are constructed based on experimental data and modified for trimmed forward flight. A FSI model that couples the one-torsional-spring-based elastic wing-hinge dynamics and unsteady flapping aerodynamics is employed, enabling precise predictions of the vortical dynamics, aerodynamic forces, and powers for a variety of flight motions. In Sec. III, we comprehensively analyze the near-field flow structures, including LEV-based and BV-based mechanisms, in a feathering wing-hinge model, as well as the flexible wing-body interaction effects on the aerodynamic force production and power consumption at various flight velocities. An extensive discussion is presented in Sec. IV, involving the robustness retained by the flexible wing hinge over broad feathering–spring stiffness conditions and external disturbances at various flight velocities. Finally, we summarize the key findings and conclusions from this study in Sec. V.

II. METHOD

A. Morphological and kinematic models

We employ the experimental data for the forward flight of *Manduca sexta* obtained in a wind tunnel by Willmott and Ellington [31,32]. A wing-body morphological model and realistic wing-body kinematics have been constructed for both hovering and five typical forward flight conditions. The

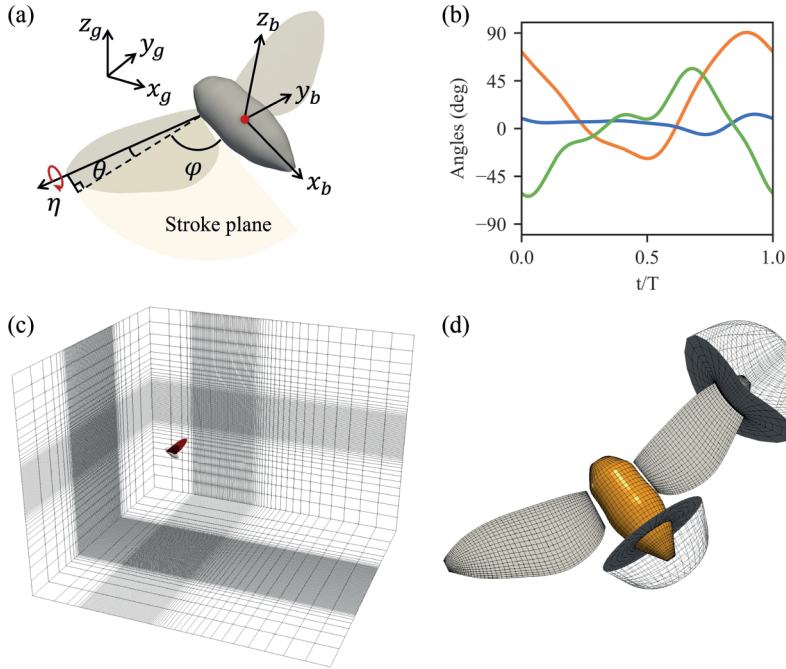


FIG. 1. (a) Schematic of wing kinematics parameters of a hawkmoth model defined in a global (x_g, y_g, z_g) and a body-fixed (x_b, y_b, z_b) coordinate systems. (b) Wing kinematics expressed as three angles: the positional angle φ (orange line), elevation angle θ (blue line), and feathering angle η (green line). (c) Multiblock and overset-grid systems of a hawkmoth CFD model comprising a background grid block, (d) a body block, and two wing blocks.

hawkmoth model has a wing length R of 50.64 mm, a body length L of 41.85 mm, and a mean chord length c_m of 18.6 mm. The wing mass m_w and the body mass m_b are 89.58 and 1995 mg, respectively. The wing kinematics are defined using three Euler angles: the positional angle φ , elevation angle θ , and feathering angle α , which are expressed in terms of the Fourier series [Figs. 1(a) and 1(b)]. The positional angle φ is the sweep angle of the projection of the rotation axis within the stroke plane, the elevation angle θ is the deviation angle between the rotation axis and the stroke plane, and the feathering angle α is the geometric angle of attack around the rotation axis. The Reynolds number for forward flight is defined as $\text{Re} = \frac{U_{\text{ref}} L_{\text{ref}}}{\nu} = \frac{V c_m}{\nu}$, where the reference velocity U_{ref} is defined as the forward speed of insects V , the reference length L_{ref} is defined as mean chord length c_m , and the air kinematic viscosity ν equals $1.5 \times 10^{-5} \text{ m}^2 \text{ s}^{-1}$. Detailed kinematic parameters of the hawkmoth wing-body model in terms of the flapping frequency f , stroke amplitude Φ , stroke plane angle χ , and body angle β_{SP} covering a broad range of flight velocities have been reported by Xue *et al.* [23], which are listed in Table I.

B. CFD wing-body model with flexible wing hinge

We developed a CFD model with flexible wing hinges, comprising a CFD wing-body insect model for computing the flapping aerodynamics and a one-torsional-spring-based elastic wing-hinge model that mimics the passive wing-pitch motion. The two models are solved in a loose-coupling manner. The CFD wing-body model is based on an *in-house* insect-inspired dynamic flight simulator [33–39]; this simulator is versatile, easily integrating the modeling of realistic wing-body geometries, realistic wing-body kinematics, and unsteady aerodynamics in flapping hovering and forward flight. A fortified finite-volume method-based Navier-Stokes solver is utilized

TABLE I. Wing-body kinematic parameters of hawk moth in hovering and forward flight [31].

Speed (m/s)	f (Hz)	Φ (deg)	χ (deg)	β_{sp} (deg)
Hovering	25.4	113.2	33.9	23.4
0.9	25.6	105.5	27.8	23.3
2.1	24.8	99.5	25.8	37.6
2.9	26.1	97.1	19.9	44.4
3.8	24.8	102.7	20.0	52.7
5.0	25.0	103.9	18.0	56.4

for incompressible flows with a dynamically moving multiblocked overset-grid system, as shown in Figs. 1(c) and 1(d). It has been verified to be self-consistent through a variety of benchmark tests capable of evaluating unsteady flapping aerodynamics in terms of vortex flows, inertial and aerodynamic forces, torques, power consumption, and energetic efficiency over a broad range of Reynolds numbers (Re) from 10^1 to 10^4 in different species [5,36,38–41]. The current model contains a four-block overset grid: a body grid ($37 \times 39 \times 9$), right-wing and left-wing grids ($39 \times 65 \times 22$), and a background grid ($165 \times 101 \times 113$) for resolving the near- and far-field vortical structures. Figures 1(c) and 1(d) depict the computational geometric models and grid systems of the CFD model.

In flapping forward flight, the aerodynamic forces F_{aero} are estimated via an integral over all the cells on the wing and body surfaces [35], in which the three force components F_x , F_y , and F_z denote the horizontal force in the direction of forward flight, the side force, and the vertical force normal to the forward velocity [23], respectively. The body-mass-specific aerodynamic powers are defined as the scalar product of velocity and the aerodynamic forces acting upon the wings and body, $P_{aero} = \sum_i (\mathbf{F}_{w,i} \cdot \mathbf{v}_{w,i} + \mathbf{F}_{b,i} \cdot \mathbf{v}_{b,i})/m_b$, and the body-mass-specific inertial powers are defined as a scalar product of velocity and the inertial force acting on the wing [35], $P_{iner} = \sum_i (m_{w,i} \mathbf{a}_{w,i} \cdot \mathbf{v}_{w,i})/m_b$, both divided by the body mass m_b [23]. Here $m_{w,i}$ is the wing mass of cell i , and $\mathbf{a}_{w,i}$ and $\mathbf{v}_{w,i}$ denote, respectively, the wing acceleration and velocity at the center of cell i . The terms $F_{w,i}$ and $F_{b,i}$ are respectively the aerodynamic forces exerted upon the wings and body, and $\mathbf{v}_{w,i}$ and $\mathbf{v}_{b,i}$ are respectively the wing velocity and body velocity at the center of cell i . The total mechanical power is thus obtained as

$$P_{total} = P_{aero} + P_{iner}. \quad (1)$$

Therefore, the periodic-averaged total mechanical power can be calculated in a wing-beat stroke as $\bar{P}_{total} = \frac{1}{T} \int_0^T P_{total} dt$. Note that the negative part of the total mechanical power throughout the wing beat is considered as the elastic storage [38], which is correlated with the elastic wing-hinge model in flapping flight.

The self-consistency of the wing-body CFD model integrated with the flexible wing-hinge model was verified and confirmed through comparisons (Fig. 2) of time-varying aerodynamic horizontal and vertical forces, as well as the pitch torque in forward flight for various cases. *Case 1*: coarse mesh (body grid: $31 \times 33 \times 7$; wing grid: $33 \times 55 \times 19$; background grid: $77 \times 85 \times 57$) with a time step of $dt = 0.0005$. *Case 2*: medium mesh (body grid: $37 \times 39 \times 9$; wing grid: $39 \times 65 \times 22$; background grid: $93 \times 101 \times 69$) with a time step of $dt = 0.0005$. *Case 3*: fine mesh (body grid: $45 \times 47 \times 11$; wing grid: $47 \times 79 \times 27$; background grid: $111 \times 121 \times 81$) with a time step of $dt = 0.0005$. Our results obviously show marginal discrepancy among the different cases.

C. One-torsional-spring-based feathering wing-hinge model

Wing rotation is accomplished by smaller muscles that directly apply a torque to the sclerites connected to the wing hinge [42]. A specific correlation between the feathering angle (η) and the pitch torque (T_η) can be observed in the features of the wing pitch, as reported using a negative

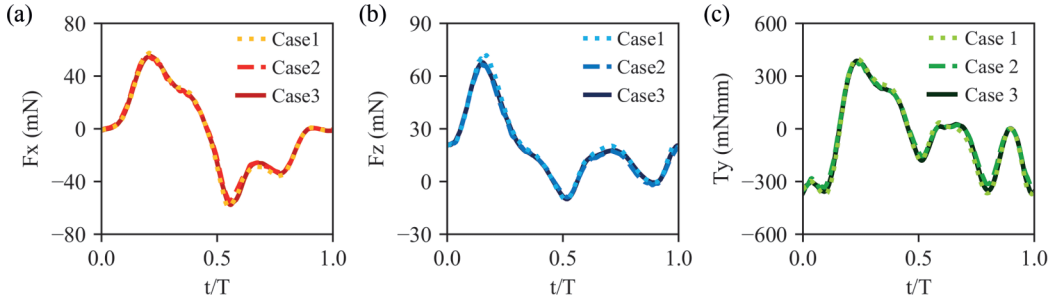


FIG. 2. Verification of grid density effect on time courses of forces and torque over a stroke cycle of forward flight at 0.9 m/s in three cases on the wing-body CFD model integrated with the flexible wing-hinge model. (a) Horizontal force F_x ; (b) vertical force F_z ; (c) pitch torque T_y .

major axis and an elliptic curve [10]. Here, we model the wing pitch with a passive-driven torsional spring [Fig. 3(a)] as

$$T_\eta = -k_\eta \eta, \quad (2)$$

where k_η denotes the feathering-spring stiffness. Considering that significant wing deformation in the chordwise direction dominates the passive wing pitch of hawkmoth, we determine the feathering-spring stiffness incorporating the wing flexibility effects based on the experimental measurements of the chordwise flexural stiffness of an insect's wings [43]. Comes and Daniel measured the chordwise flexural stiffness EI versus chord length c_m in 16 insect species including hawkmoth *Manduca* and reported a quantitative relation between the two terms as $y = 2.01x - 1.8$ in a logarithmic scale [43]. Since the spring constant given by $k = EI/L_{\text{ref}}$ can be set as the macroscopic torsional stiffness of the insect wing [24], we then calculate the feathering-spring stiffness k_η (Nm) by dividing the chordwise flexural stiffness EI (Nm^2) with the reference length L_{ref} as mean chord length c_m (m), such as $k_\eta = \frac{EI}{L_{\text{ref}}} = \frac{10^{-1.8} c_m^{2.01}}{L_{\text{ref}}}$. By substituting the morphological data of the real hawkmoth in our study, $c_m = 18.6 \times 10^{-3}$ m, we finally obtain the stiffness coefficient $k_\eta = 2.83 \times 10^{-4}$ Nm, which is also in reasonable agreement with the experimental measurements of nine hawkmoth individuals within a predicted range of $1.34 \times 10^{-4} \sim 5.38 \times 10^{-4}$ Nm [5,43].

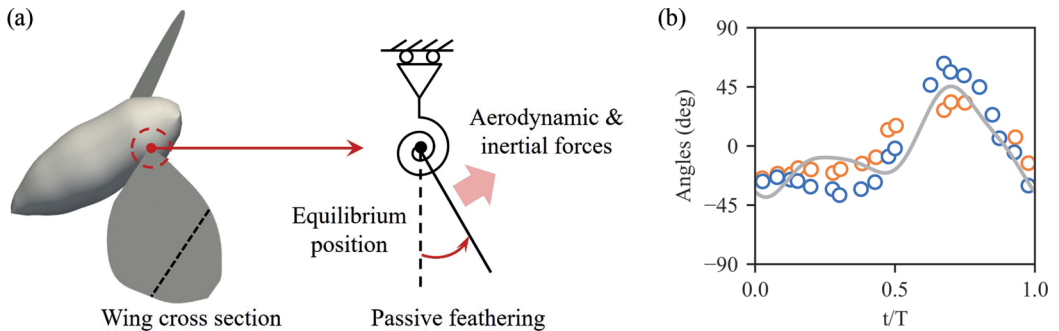


FIG. 3. (a) Schematic view of a one-torsional-spring-based flexible wing hinge corresponding to the wing-pitch motion [1]. (b) Time course of feathering angles in a stroke cycle from experimental observations [31] (open circles) and the flexible wing-hinge model-based prediction (solid line). The measured feathering angles at a forward flight speed of 2.1 m/s are grouped into the mean angles for the inner (red circle) and outer (blue circle) functional wing sections [31].

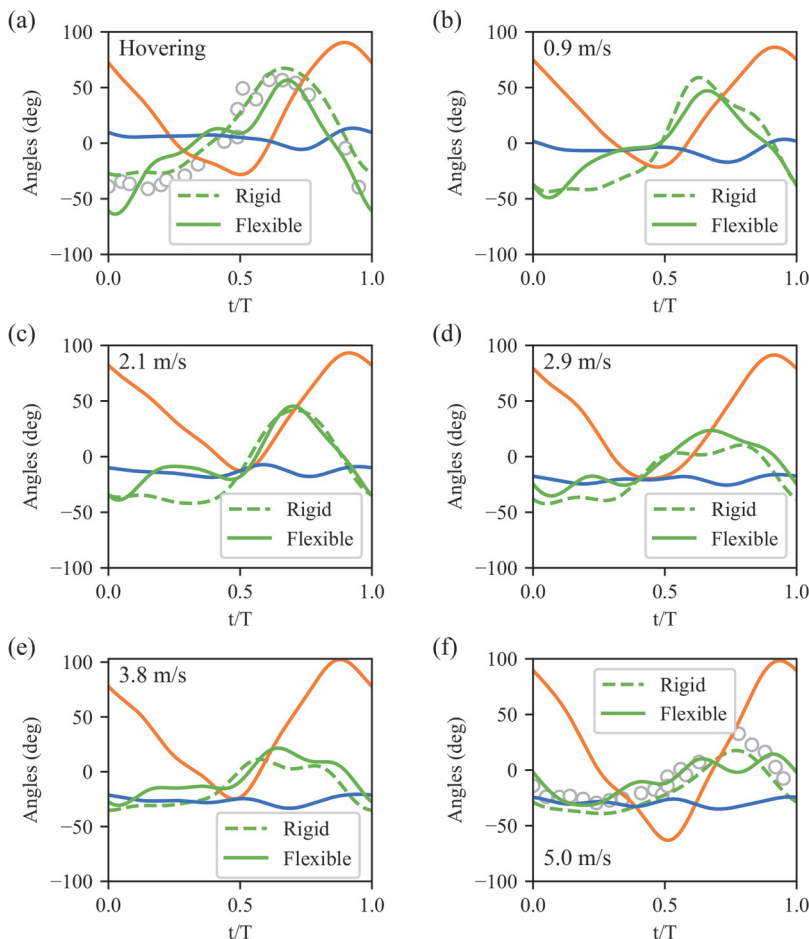


FIG. 4. Wing kinematics of a hawkmoth model with flexible (solid line) and rigid wing hinges (dashed line) during (a) hovering flight and forward flight at (b) 0.9 m/s, (c) 2.1 m/s, (d) 2.9 m/s, (e) 3.8 m/s, and (f) 5.0 m/s. Three angles are presented: positional angle φ (orange), elevation angle θ (blue), and feathering angle η (green). Open circles represent the experimental observations [31] of feathering angles in a stroke cycle during hovering and fast forward flight of the hawkmoth. Dashed lines represent the wing kinematics of the rigid hawkmoth model of hovering and five forward flights, obtained computationally during the trimming process based on a genetic algorithm embedded within a CFD-driven model [23]. Flow chart of the approach to determine trimmed flights of the rigid model are illustrated and described in detail in Xue *et al.* [23].

Given the aim in the current study to investigate the flexible wing-hinge-driven aerodynamics and energetics in comparison with those of our previous rigid wing-body model [23], the initial feathering angles were prescribed the same as the trimmed wing kinematics of the rigid wing-body model [23], then the feathering angles in the flexible wing-hinge model were determined based on the interactions owing to the flapping-wing motion, the unsteady aerodynamics, and the inertial forces and torques, which eventually converged to a stable situation in at least five stroke cycles. The time course of feathering angles in a stroke cycle at a slow forward flight speed of 2.1 m/s are depicted based on experimental observations in a wind tunnel [31] and the flexible model-based results. The feathering angle based on the elastic wing-hinge model matches the measured wing kinematics well [Fig. 3(b)]. An extensive comparison of the feathering angles (Fig. 4) among the flexible and rigid models and the measurements is described in Sec. III A. The consistency between

the flexible wing-hinge model-based prediction and the measurements is reasonable, showing some differences of the mean values less than 2° in hovering, slow (0.9 and 2.1 m/s), and fast (5.0 m/s) flights whereas there are relatively pronounced differences for 2.9 m/s (9°) and 3.8 m/s (6°). On the other hand, we also see that the differences in the root-mean-square values of feathering angles between the predictions and measurements at all flight velocities show a 35% reduction in the flexible wing-hinge models (4.8°) rather than the rigid models (7.4°). This indicates that the flexible model using elastic wing hinge can result in time-varying feathering angles closer to those of a real hawkmoth in hovering, slow, and fast forward flights, which lends credence to the use of an elastic wing hinge.

D. Modeling of external disturbances

In this study, the one-torsional-spring-based elastic wing-hinge model for mimicking the passive wing-pitch motion is introduced into the flapping-wing dynamic model for free-flight insects with prescribed positional and elevation angles. The interactions among the flapping-wing motion, unsteady aerodynamics, and inertial forces and torques further determine and alter the feathering angle. The governing equation for the flapping-wing dynamics is given as

$$(B_{2w} - C_w) \frac{d\omega_{0b}}{dt} - M_{b2w} = {}_bM_a + M_k - a_2 - b_2 + c, \quad (3)$$

where ω_{0b} denotes the angular velocity of the flapping wing, M_{b2w} is a variable representing the torque between the thorax of the body and the flapping wings, ${}_bM_a$ is the aerodynamic torque, and M_k denotes the torque due to the torsional spring with respect to the wing hinge. Here, B_{2w} , C_w , a_2 , b_2 , and c are coefficients given by [10]

$$B_{2w} = -m_w [R_h]_\times [R_{wg}]_\times + E_{w2b} I_w E_{b2w}, \quad (4)$$

$$C_w = -m_w [R_h]_\times [R_h + R_{wg}]_\times, \quad (5)$$

$$a_2 = m_w (R_h + R_{wg}) \times (-{}_b g), \quad (6)$$

$$b_2 = m_w R_h \times [\omega_{0b} \times (\dot{E}_{w2b} E_{b2w} R_{wg})] + \dot{E}_{w2b} I_w E_{b2w} \omega_{0b} + E_{w2b} I_w \dot{E}_{b2w} \omega_{0b}, \quad (7)$$

$$c = m_w [R_h]_\times [\omega_{0b}]_\times (\dot{E}_{w2b} E_{b2w} R_{wg}) - m_w R_h \times {}_b g - R_h \times {}_b F_a, \quad (8)$$

in which \times denotes the cross product of vectors or matrices, ${}_b g$ represents gravitational acceleration in the body-fixed frame, and $[\cdot]_\times$ denotes the cross-product matrix defined as

$$[a]_\times = \begin{bmatrix} 0 & -a_3 & a_2 \\ a_3 & 0 & -a_1 \\ -a_2 & a_1 & 0 \end{bmatrix}. \quad (9)$$

Here, m_w is the wing mass, I_w is the wing moment of inertia, R_h is the position of the wing hinge with respect to the body's center of mass (CoM), ω_{0b} denotes the angular velocity of the flapping wing, E_{w2b} is the coordinate transformation matrix from the wing-fixed frame to the body-fixed frame, E_{b2w} is the coordinate transformation matrix from the body-fixed frame to the wing-fixed frame, R_{wg} is the position of the wing's CoM with respect to the wing hinge, and ${}_b F_a$ denotes the aerodynamic force. The relation between the three Euler angles and the angular velocity of the wing can be written as

$$E_{sp2b} E_{dEuler2sp} \begin{pmatrix} \dot{\varphi} \\ \dot{\theta} \\ \dot{\eta} \end{pmatrix} = \omega_{0b}, \quad (10)$$

where E_{sp2b} is the coordinate transformation matrix from the stroke plane frame to the body-fixed frame and $E_{dEuler2sp}$ is the coordinate transformation matrix that transfers the time derivative of the three angles to the stroke plane frame. With the initial positional φ , elevation θ , and feathering angles η , the flapping-wing motion can be further determined based on the following equation:

$$\dot{E}_{dEuler2sp}^{-1} E'_{sp2b} \omega_{0b} + E_{dEuler2sp}^{-1} E'_{sp2b} \dot{\omega}_{0b} = \begin{pmatrix} \ddot{\varphi} \\ \ddot{\theta} \\ \ddot{\eta} \end{pmatrix}. \quad (11)$$

Considering that flying insects are frequently affected by external disturbances, such as gusts of wind or raindrops in nature, it is of great significance to investigate the insect's external disturbance-rejection ability in terms of aerodynamic performance and flight stability. We now develop a FSI model to examine how the passive wing pitch alters the robustness of the hawkmoth's forward flight by applying a force impulse to the wing's CoM at mid-downstroke within a period of $0.1T$ and with a magnitude of $150m_w$, while keeping the insect body locked in a tethered flight mode. The magnitude of the force impulse specified for hawkmoth forward flight is determined based on external disturbance-rejection experiments relating to bumblebee hovering flight [10] using a force impulse of $1500m_w$. Considering that there exists an $O(10^1)$ magnitude difference between the wing-to-body mass ratios of the hawkmoth and bumblebee, a force impulse of $150m_w$ is sufficient to induce an impactful dynamic response for the hawkmoth model with flexible wing hinges. The flapping-wing dynamics under external disturbances can be further modeled on the basis of Eq. (3) by adding perturbations such as

$$(B_{2w} - C_w) \frac{d\omega_{0b}}{dt} - M_{b2w} = {}_bM_a + M_k + M_p - a_2 - b_2 + c, \quad (12)$$

where the perturbation term is added as the external torque M_p due to the force impulse acting on the two wings. For instance, a vertical force impulse is applied on the wing's CoM within a period of $0.1T$ with a magnitude of $150m_w$, thus the instantaneous external force on a single wing in the body-fixed frame can be written as

$${}_bF_p = 150E_{g2b}m_w g, \quad (13)$$

where m_w is the wing mass, ${}_g g$ represents gravitational acceleration in the ground frame, and E_{g2b} is the coordinate transformation matrix from the ground frame to the body-fixed frame. The instantaneous external torque in the body-fixed frame of a single wing is defined as

$$M_p = (R_h + R_{wg}) \times {}_bF_p, \quad (14)$$

which is applied at time instant of t_p lasting for a period of $0.1T$, with the time integration in a wing-beat stroke as

$$M_{p,T} = \int_{t_p}^{t_p+0.1T} (R_h + R_{wg}) \times {}_bF_p dt. \quad (15)$$

Here R_h is the position of the wing hinge with respect to the body's CoM and R_{wg} is the position of the wing's CoM with respect to the wing hinge. The dynamic response of the flapping-wing kinematics and the aerodynamic performance of vertical force production following different perturbations can now be determined by integrating Eqs. (3)–(15).

III. RESULTS

A. Flexible wing-hinge-driven feathering motion

The wing kinematics of the feathering angle based on the elastic wing-hinge model are determined by the interactions among the flapping-wing motion, unsteady aerodynamics, and inertial forces and torques. Thus, we first compare the flexible wing-hinge-driven feathering motion in

various hovering and forward flight velocities with those of the rigid wing kinematics (Fig. 4). The positional angles, elevation angles, and initial feathering angles of the flapping wings are prescribed at all flight velocities based on the trimmed wing kinematics of the rigid wing-body model in stable flight conditions [23]. This allows us to discuss the flexible wing-hinge-driven effects on the aerodynamics in comparison with our previous study of a rigid wing-body model [23]. The model-based predictions of flexible feathering angles tend to present lower mean values in hovering flight and higher mean angles in fast forward flight compared to the rigid wing kinematics [Figs. 4(a) and 4(f)]. We further examined the mean value differences of feathering angles between flexible and rigid model-based feathering angles and the wind-tunnel measurements [31]. The consistency between the flexible wing-hinge model-based results and the measurements are reasonable, showing some differences of the mean values less than 2° in hovering, slow (0.9 and 2.1 m/s), and fast (5.0 m/s) flights while relatively pronounced differences for 2.9 m/s (9°) and 3.8 m/s (6°). On the other hand, we also see that the differences in the root-mean-square values of feathering angles between the predictions and measurements at all flight velocities show a 35% reduction in the flexible wing-hinge models (4.8°) rather than the rigid models (7.4°). This indicates that based on the trimmed modeling, the flexible model-based feathering motions are in better agreement with those of real hawkmoth flight in comparison with the rigid model [23].

There is a noticeable discrepancy between the down- and upstroke that the lower and flatter feathering angles are observed in the flexible wing-hinge model rather than the rigid ones during the downstroke, despite the consistent variations appearing in both the rigid and the flexible models during the upstroke. According to the experimental observations of Willmott and Ellington [31], the plateau in the downstroke feathering angle may be due in part to the longer duration of the downstroke translational phase, especially for *Manduca sexta*. The discrepancy between the two half-strokes is likely to result from the asymmetric resistance to pronatory and supinatory rotation, which is inherent in insects' wings [31,44]. The advanced wing rotation during supination at slow forward flight speeds of 0.9 and 2.1 m/s obviously results in high angles of attack, which may enhance the production of lift and drag forces during the downstroke. This advanced pitch motion was also observed in the simulation-based study of hovering flight of dipteran [24]; the flexible wing turned to twist immediately before the wing reversal, and thus is responsible for enhancing the production of lift force [25] owing to the intense LEV coherently attached on the wing surface [24]. Thus, the flexible wing-hinge-driven feathering motion in association with forward flight can also generate the advanced pitch motion, hence producing more aerodynamic forces. Further investigations on the underlying mechanisms of flexible wing hinges on the aerodynamics in various forward flights are provided in Sec. III B.

B. Forward flight aerodynamics with flexible wing hinge

The unsteady aerodynamics associated with flexible wing-body interaction at various forward flight velocities are now investigated in terms of the vertical force production. For comparison, the near-field flow structures of two hawkmoth models with flexible and rigid wing hinges in slow and fast forward flights are illustrated in Fig. 5.

The isosurface of the Q criterion [45] with $Q = \frac{1}{2}(\|\Omega\|^2 - \|S\|^2) > 0$ is employed to identify the vortex structures, where $S = \frac{1}{2}[\nabla u + (\nabla u)^T]$ and $\Omega = \frac{1}{2}[\nabla u - (\nabla u)^T]$ are the strain rate and vorticity tensors, respectively, and u denotes the velocity vector. For illustration, the nondimensional Q criterion in Fig. 5 is 0.2. The rotational directions of vorticity are illustrated via color mapping by utilizing the normalized helicity density. The simulated flow patterns for hawkmoth forward flight in terms of the wing-based leading-edge vortex in structure and location are consistent with the experimental observations made by smoke trail [46] and digital particle image velocimetry techniques [13]. Our simulations with flexible and rigid models thus clarify the attachment and detachment nodes of the LEV-like structures above the thorax, as suggested in the experimental study of the forward flight of a tethered hawkmoth by Bompfrey *et al.* [13]. However, there are discrepancies in terms of the size and strength of the vortex structures between the flexible and rigid

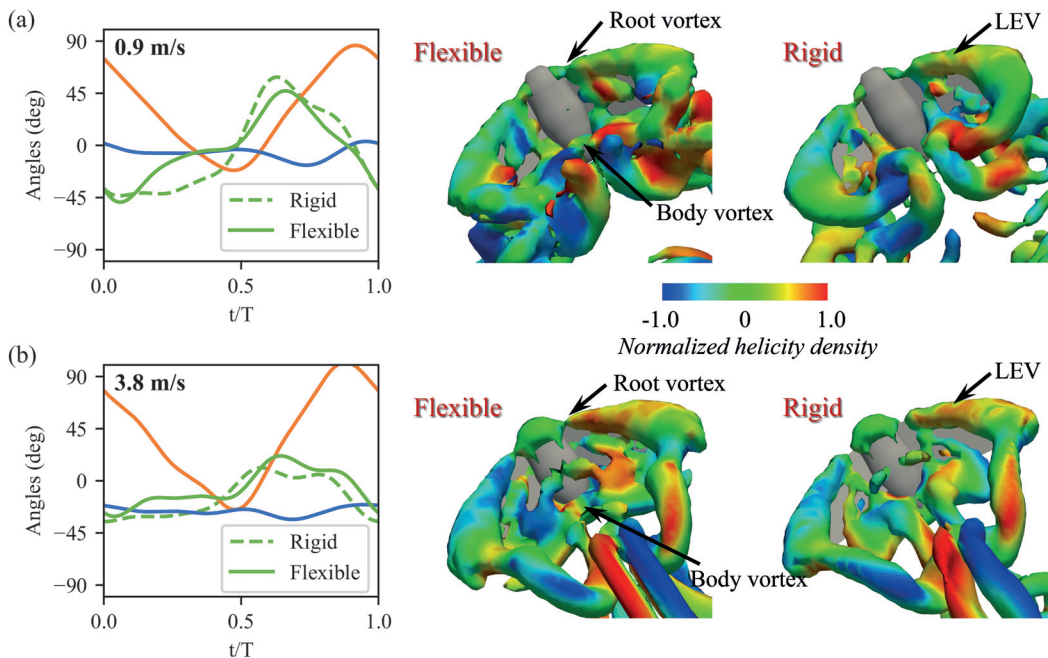


FIG. 5. Wing kinematics and near-field flow structures of a hawkmoth model with flexible (solid line) and rigid wing hinges (dashed line) in (a) slow forward flight of 0.9 m/s and (b) fast forward flight of 3.8 m/s.

models. The root vortex (RV) of the flexible model in the vicinity of the wing base between the LEVs and the head vortex is apparently strengthened in slow and fast forward flights. This may be attributable to the high angle of attack at mid-downstroke. Moreover, the BVs, including the thorax vortex and the rear-body vortex, are larger in the flexible wing-hinge model, particularly at the fast flight velocity [Fig. 5(b)]. The LEV and BV features indicate that the wing-body interaction due to the flexible wing hinge may enhance the flapping aerodynamic performance.

The effects of the flexible wing hinge on aerodynamic performance in various forward flights are now examined by investigating the correlations between the featured LEVs, BVs, and RVs and the vertical force production. In Fig. 6, the time courses of vertical force are plotted and compared between rigid and flexible wing-hinge models at flight speeds of 0.9 m/s (slow flight) and 3.8 m/s (fast flight), along with the wing-surface pressure distributions and instantaneous streamlines visualized at instants of vertical force peak in the first half-downstroke. The first vertical force peak occurs early in the downstroke in both the slow and fast flight conditions, corresponding with the conical downstroke LEV. Through comparisons between the rigid and flexible wing-hinge models, a larger negative pressure area with lower pressure values appears on the wing surface of the flexible wing-hinge model while showing greater magnitudes of absolute flow velocity at leading edge in both slow and fast flights. This is the result of the enhanced downstroke leading-edge vortex in the flexible model. Given the advanced wing rotation observed in the flexible model in the early downstroke (Fig. 4), which leads to a larger angle of attack, a more intense LEV is observed on the flexible model [5], resulting in a rapid increase and a single peak in the vertical force (Fig. 6).

A pronounced increase exists in the time-varying body-based vertical forces on the flexible model at forward flight speeds of 0.9 and 3.8 m/s (Fig. 7): the greatly increased force peak is apparently a result of the greatly enhanced BVs during the first half-downstroke together with the thorax vortex (TXV) and rear-body vortex (RBV). In our study, the fortified finite-volume method-based Navier-Stokes solver for incompressible flows with a dynamically moving multiblocked overset-grid system is versatile and robust [5,36,38–41] capable to deal with the problem of wing-body interaction

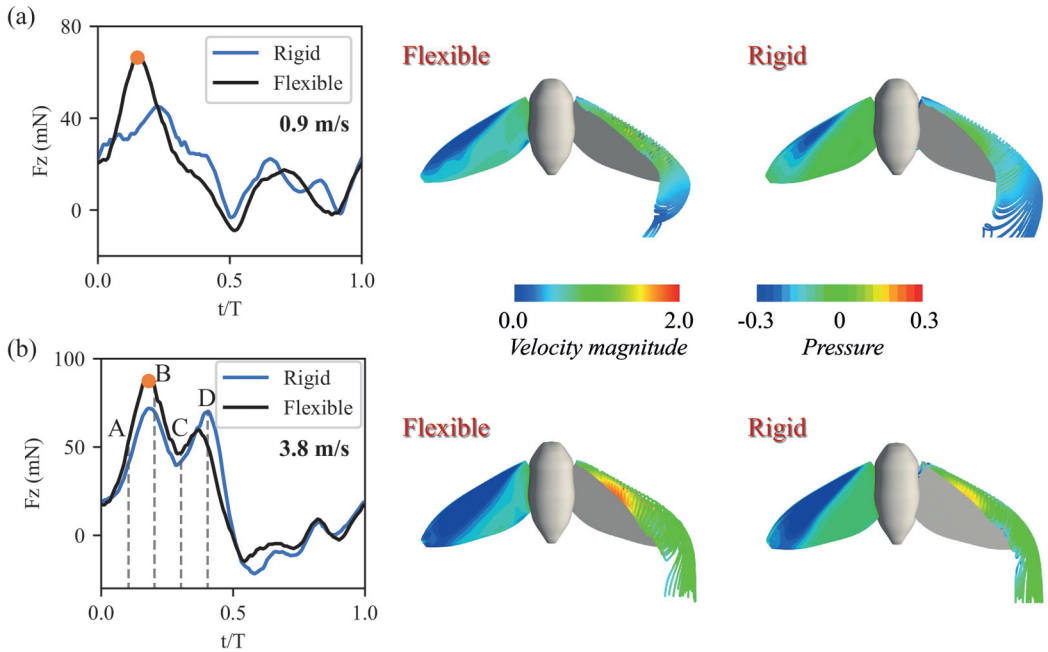


FIG. 6. Time course of vertical force and distributions of wing-surface pressures and instantaneous streamlines of a hawkmoth model with flexible and rigid wing hinges in (a) slow forward flight of 0.9 m/s and (b) fast forward flight of 3.8 m/s at instants of force peak in the first half-downstroke.

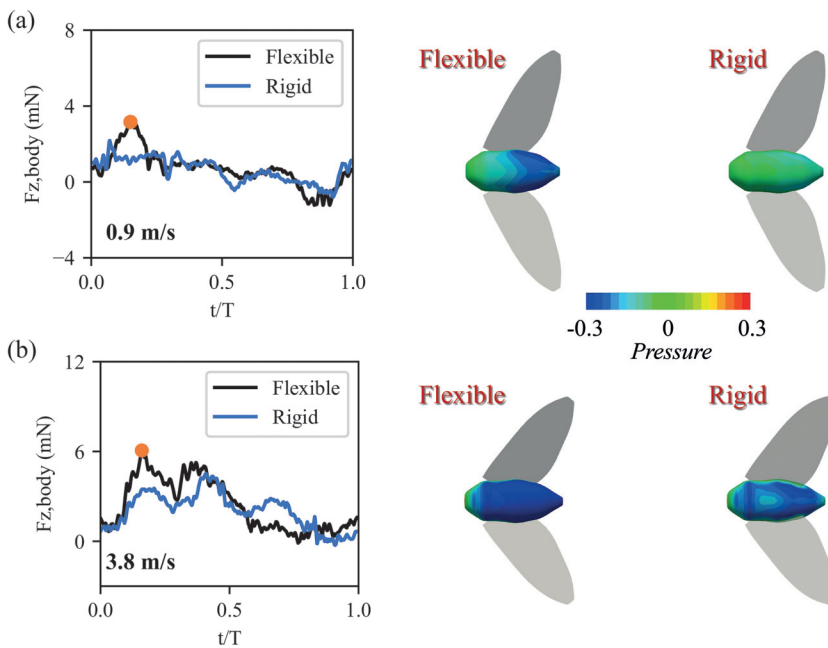


FIG. 7. Time course of body-based vertical force and pressure distributions on the body surface of a hawkmoth model with flexible and rigid wing hinges in (a) slow forward flight of 0.9 m/s and (b) fast forward flight of 3.8 m/s at instants of force peak in the first half-downstroke.

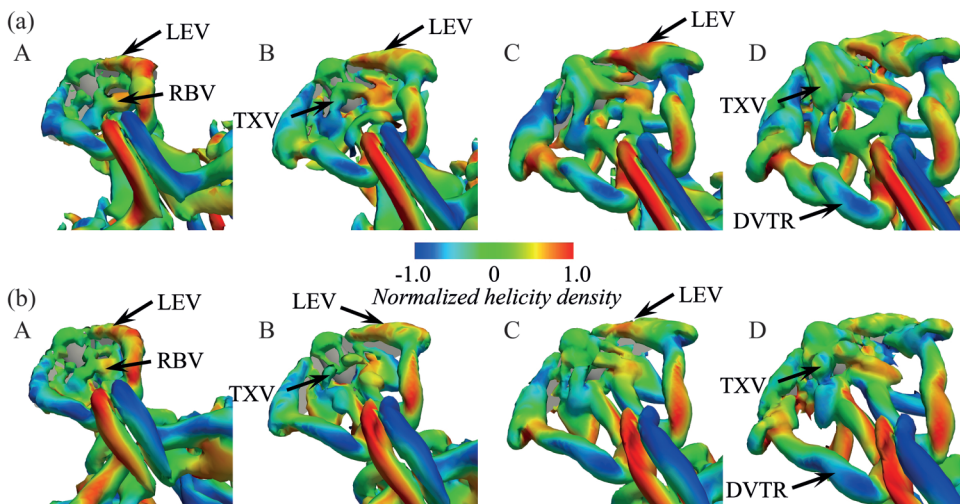


FIG. 8. Illustration of near-field vortex dynamics of a hawkmoth model with flexible (a) and rigid (b) wing hinges at four instants [Fig. 6(b)]: $t/T = 0.1$ (A), 0.2 (B), 0.3 (C), and 0.4 (D) in fast forward flight of 3.8 m/s.

even when they touch upon each other, which is often observed in insect flight [31]. In this study, there actually existed some limited portions in a wing-beat stroke when the wing touches the body, resulting in an overlapping region between them. Our Navier-Stokes solver and wing-body model, however, could successfully resolve the problem, achieving a stable numerical convergence and computing the flow fields (velocity and pressure) reasonably [35]. Because some meshes on the wing overlap with the body, the aerodynamic forces acting on the wing and body, which are integrated throughout the surfaces of the two wings, and the body displays some noticeable variations in a time-varying feature. Our results indicate that such phenomenon may happen in realistic insect flights but hardly alter the aerodynamic force production leaving merely a slight variation in vertical force.

We further examine the correlations between the vortex dynamics and the vertical force production through visualization of the flow structures (Fig. 8) at four instants: $t/T = 0.1$ (A), 0.2 (B), 0.3 (C), and 0.4 (D) marked in Fig. 6(b) with the nondimensional Q criterion as 0.05 . At the early downstroke ($t/T = 0.1$), a horseshoe vortex appears comprising a trailing-edge vortex, a LEV, and a tip vortex wrapping the flapping wing. A rear-body vortex then is observed at wing base, bridging the LEVs of the paired flapping wings over the upper surface of the body, and further merging with a head vortex (Fig. 8, A). Eventually a downstroke vortex tube ring (DVTR) is formed. As the LEVs grow in strength and size at mid-downstroke ($t/T = 0.1$) (Fig. 8, B), the first wing-based [Fig. 6(b)] and body-based force [Fig. 7(b)] both reach higher peaks in the flexible wing-hinge model corresponding to more intense LEVs [Fig. 6(b)] and rear-body vortex [Fig. 7(b)] than the rigid model. The rear-body vortex moves backward, splitting into two spiral vortex tubes attached onto the aft of the body. In addition, an intense thorax vortex is observed at the thorax (Fig. 8, B), connecting to the head vortex and the rear-body vortex and presents a fast growth in strength (Fig. 8, C), resulting in the second body-based vertical force peak [Fig. 7(b)]. The stronger thorax vortex on the flexible wing-hinge model during the late downstroke ($t/T = 0.3, 0.4$) (Fig. 8, C and D) produces higher body-based vertical force [Fig. 7(b)] while the DVTR elongates with an inclination from the horizontal direction at the late downstroke ($t/T = 0.4$) (Fig. 8, D). We then infer that the wing-body interaction with the elastic wing hinge is likely to augment the aerodynamic force production at all forward flight velocities.

The wing-body interaction due to the elastic wing hinge is further examined by investigating the vorticity contours in the vicinity of the wing root. These are visualized on two cutting planes at a

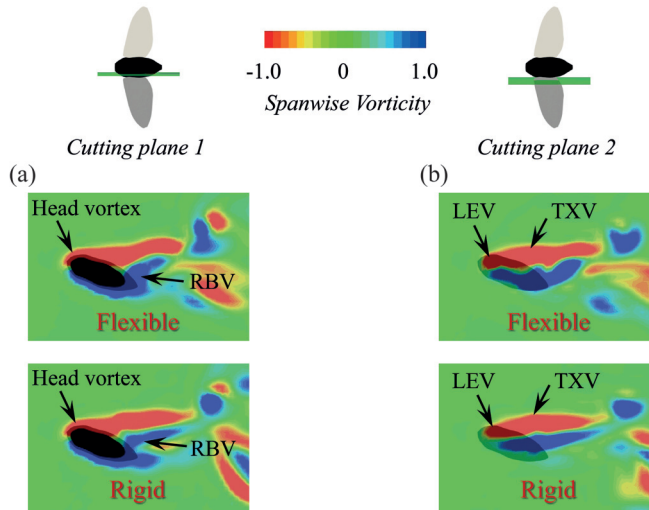


FIG. 9. Vortex topologies in the vicinity of the wing root for hawkmoth models with flexible and rigid wing hinges in fast forward flight of 3.8 m/s. Vorticity contours are visualized on two cutting planes located at (a) $0.3c_m$ (cutting plane 1) and (b) $0.6c_m$ (cutting plane 2) away from the symmetry plane of the insect's body. Detailed topologies are illustrated in terms of the head vortex, leading-edge vortex (LEV), rear-body vortex (RBV), and thorax vortex (TXV).

fast forward flight velocity of 3.8 m/s in Fig. 9. On cutting plane 1, the head vortex and thorax vortex are attached coherently onto the body surface, while the RBV on the posterior of the body has greater vorticity in the flexible model [Fig. 9(a)]. This corresponds to the enhanced body-based vertical force peak shown in Fig. 7(b). On cutting plane 2, a RV along with the LEV and thorax vortex is present reinforced on the flexible model [Fig. 9(b)]. Since the BV is proven attributed to the strengthened LEV in the vicinity of the wing root in the chordwise direction [23], which is consistent with the simultaneously strengthened vortical structures [Fig. 8(a)] as well as the wing- and body-based vertical forces [Figs. 6(b) and 7(b)], the flexible wing hinge thus plays an important role in enhancing the interplay between LEVs and the body vortex at fast forward flights.

To examine the velocity dependency in association with the effects of the flexible wing hinge on the body-based vertical force, Fig. 10 shows the cycle-averaged body-based aerodynamic forces with respect to the forward flight velocity. The flying body obviously produces a velocity-dependent vertical force, showing a remarkable increase with increasing flight velocity of up to 14.5% of the

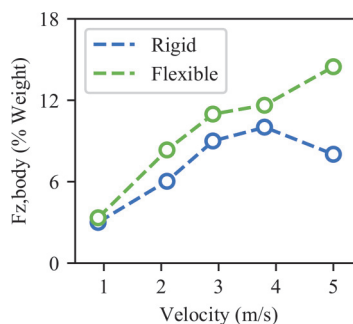


FIG. 10. Percentages of cycle-averaged body-based vertical forces with respect to the weight of the hawkmoth against the forward flight velocity with rigid wing hinge (blue) and flexible wing hinge (green).

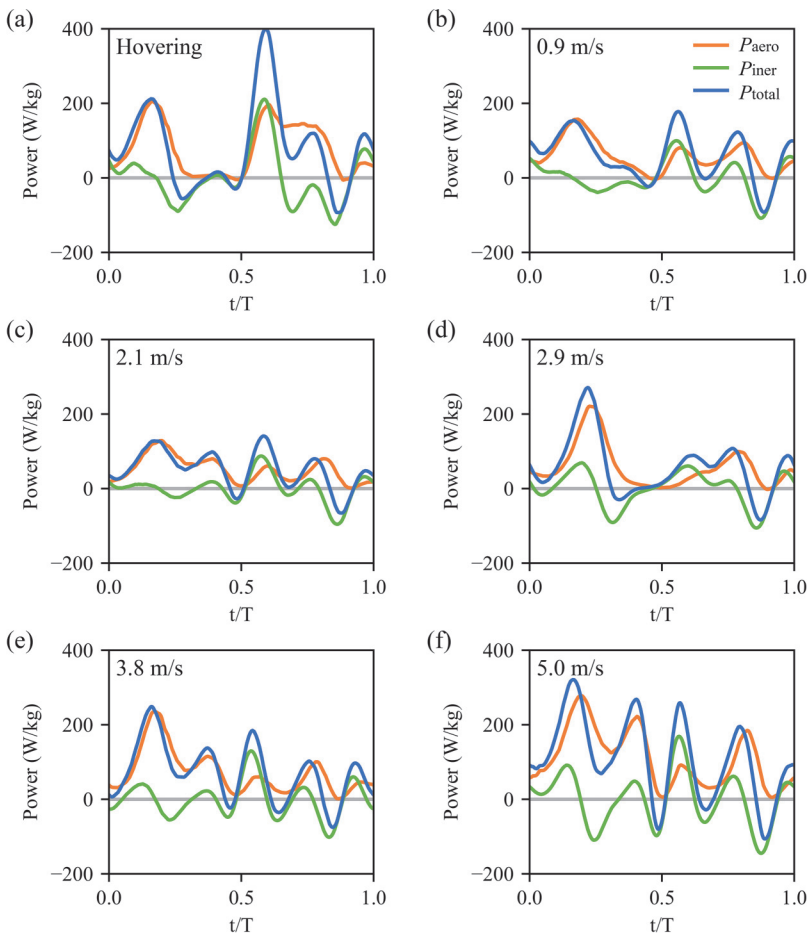


FIG. 11. Time courses of body-mass-specific aerodynamic, inertial, and total mechanical powers during (a) hovering and forward flight at (b) 0.9 m/s, (c) 2.1 m/s, (d) 2.9 m/s, (e) 3.8 m/s, and (f) 5.0 m/s.

hawkmoth's weight at a fast forward flight speed of 5 m/s. Corresponding to the reinforced vortex structures shown in Fig. 8, the flexible wing hinge enables additional aerodynamic force production at all flight velocities, with a maximum increase of 6.5% compared with the rigid wing-hinge model at the fastest flight speed (Fig. 10).

C. Forward flight energetics with flexible wing hinge

The energetics with a flexible wing hinge at various forward flight velocities are evaluated in terms of power cost and efficiency. Figure 11 shows the inertial, aerodynamic, and total power components in a wing-beat cycle in terms of body mass. The aerodynamic power P_{aero} required to overcome air drag remains positive throughout a complete wing beat, while the inertial power P_{iner} for accelerating or decelerating the wing takes both positive and negative values. The sum of the aerodynamic and inertial powers is the total mechanical power P_{total} , which is negative during the deceleration phase, mostly in the late down- and upstroke (Fig. 11), when less power is required to overcome the inertial forces [35].

The negative works during both hovering and forward flight can be explained as an elastic-energy storage mechanism within the flexible wing hinge. As a set of tiny, highly specialized synchronous

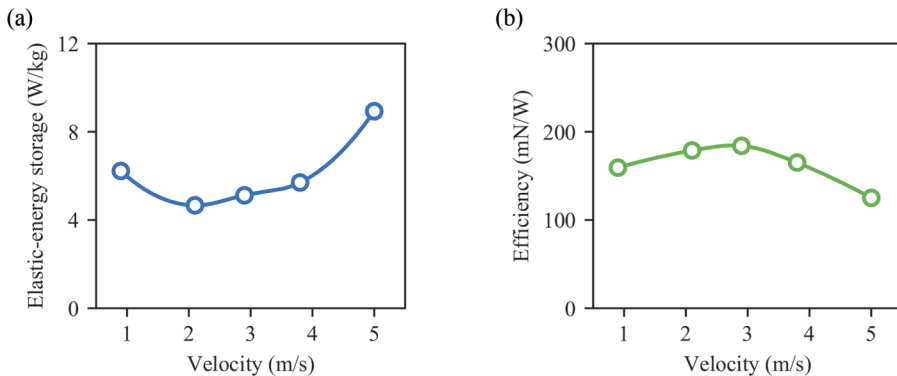


FIG. 12. (a) Elastic-energy storage and (b) power efficiency of a flapping hawkmoth with flexible wing hinge at various flight velocities.

muscles are directly inserted within the wing hinge, the flexible wing hinge can store excessive inertial power during wing decelerating and recover this energy during wing acceleration [47]. The negative portion is reported to constitute 11.5% of the total work for fruit flies, 9.4% for bumblebees, and 12.9% for simulated hawkmoths during hovering flight [38]. Here, we estimate the negative power (elastic storage) of the hawkmoth model with a flexible wing hinge at various forward flight velocities. The correlations between the time-averaged, body-mass-specific elastic-energy storage and the flight velocity are depicted in Fig. 12(a), in which the power curve is J shaped. The minimum energy storage (4.7 W/kg) occurs during slow forward flight at 2.1 m/s, while high elastic storage occurs during both hovering (6.2 W/kg) and fast forward flight (8.9 W/kg). The elastic storage-based energy saving at various flight velocities drops within a range of 7%–10% of the total power consumption. This is consistent with measurements of a fruit fly hovering (10% energetic cost reduction [48]) and a flapping blowfly (6% of inertia power requirement based on the wing deformation [49]). The power efficiency of the flapping hawkmoth with a flexible wing hinge, defined as $e = F_z/P_{\text{total}}$, is plotted in Fig. 12(b) for various flight velocities. Here, the negative power owing to elastic-energy storage is accounted for when estimating the time-averaged total mechanical power consumption, resulting in a noticeably high (optimal) power efficiency at intermediate flight velocities.

IV. DISCUSSION

A. Aerodynamic robustness

We now discuss the aerodynamic robustness of hawkmoth flight with a flexible wing hinge, focusing on the feathering-spring stiffness dependency. The feathering-spring stiffness dependency is investigated in terms of the feathering angle amplitude, vertical force production, power cost, and efficiency over a broad range of forward flight velocities with five different stiffnesses of $k = [0.1, 0.3, 1, 3, 10]k_0$, where k_0 is the realistic feathering-spring stiffness based on experimental measurements [43].

As shown in Fig. 13(a), the feathering amplitude decreases with increasing feathering-spring stiffness at all flight velocities, but decreases with increasing flight velocity; for example, under the weak stiffness of $k = [0.1, 0.3]k_0$, there is a maximum variation of 75° in fast flight at 3.8 m/s, increasing to 136° at the low velocity of 0.9 m/s. This velocity-dependent variation in feathering amplitude shrinks significantly with increasing feathering-spring stiffness, eventually showing almost no discrepancy at the largest stiffness of $k = 10k_0$. This phenomenon of the feathering angle having a smaller amplitude at fast flight velocities has been observed in the realistic wing kinematics of hawkmoth flight at various forward velocities [31]. The feathering angle due to passive pitch

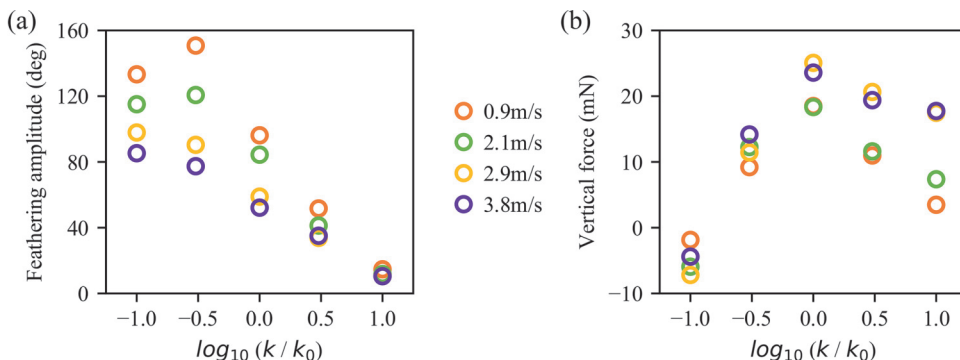


FIG. 13. Feathering amplitude (a) and mean vertical force (b) versus feathering-spring stiffness at various flight velocities ($k = [0.1, 0.3, 1, 3, 10]k_0$).

rotation is dominated by the flapping aerodynamics [10], and slow flights including hovering are more sensitive to the flexible wing hinge generating larger feathering angles (angles of attack) for sufficient lift production, whereas lower feathering angles create sufficient lift forces in fast forward flight. Moreover, the results indicate that adjusting the stiffness of the flexible wing hinge may enable optimal flapping aerodynamic performance for various flight modes during hovering, slow, and fast flight. For instance, as reported in [42,50], the flapping wing rotation can be directly related to the bending stiffness of the flexible hinge when conducting a takeoff maneuver, resulting in pronounced stiffness differences during the transition from hovering to slow flight and then to fast forward flight.

The association between the vertical force and the feathering-spring stiffness is illustrated in Fig. 13(b): the vertical force exhibits an upside-down V-shape curve, reaching a peak at the measurement-based feathering hinge stiffness, k_0 , and achieving optimal aerodynamic force production at all flight velocities. An extensive study has verified that large vertical forces can be produced robustly in the vicinity of the realistic stiffness k_0 , with less than 0.1% variation when the stiffness k varies in the range $\pm 5\% k_0$. The results indicate that the realistic hinge stiffness enables optimal and robust aerodynamic performance associated with vertical force production.

Further investigation of the feathering-spring stiffness dependency is now undertaken in terms of the power consumption and efficiency over a broad range of the stiffness and flight velocity. As depicted in Fig. 14(a), the periodic-averaged total mechanical power is remarkably low at the weak stiffness for all flight velocities. This may be ascribed to the large elastic-energy storage,

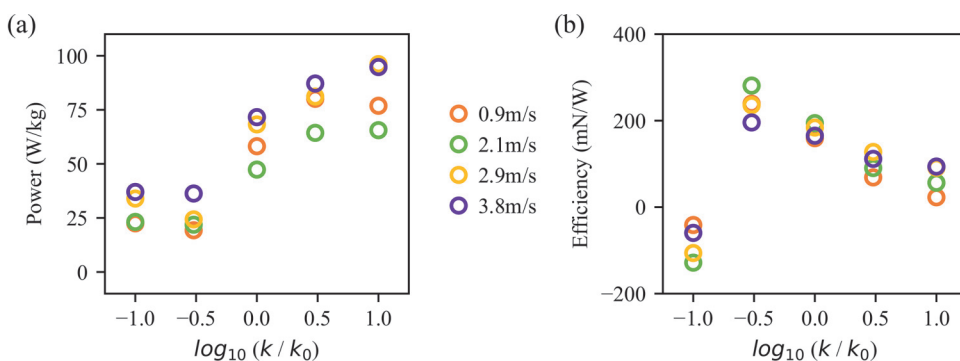


FIG. 14. Periodic-averaged total mechanical power (a) and power efficiency (b) versus feathering-spring stiffness at various flight velocities.

which diminishes the power cost through the highly flexible wing hinges. The power efficiency ($e = F_z/P_{\text{total}}$) at various flight velocities [Fig. 14(b)] declines over a broad range of the feathering-spring stiffness (from $0.3k_0$ to $10k_0$). Interestingly, the power efficiency shows a peak when the stiffness is slightly lower than the realistic value ($0.3k_0 < k < k_0$), corresponding to the relatively high vertical force [Fig. 13(b)] and low power cost [Fig. 14(a)] at all flight velocities. This phenomenon can be attributed to an exceptional case with “very flexible” wing hinges ($k = 0.1k_0$), in which the aerodynamic performance has a negative periodic-averaged vertical force and abnormal power cost. This leads to a noticeable chasm in power efficiency at $0.1k_0 < k < 0.3k_0$, forcing the stiffness band $0.3k_0 < k < k_0$ to be in the optimal range. Thus, the results demonstrate that the realistic wing-hinge stiffness is capable of achieving optimal aerodynamic force production while obtaining high power efficiency at various forward flight velocities.

B. External disturbance-rejection robustness

External disturbances from the natural environment, such as gusts of wind or raindrops, may remarkably alter the aerodynamic performance and flight stability of flying insects. Here, we investigate the external disturbance-rejection robustness of a hawkmoth’s forward flight with the flexible wing hinge at various flight velocities. The FSI model [Eqs. (3)–(15)] is used to examine the features of external disturbance rejection under a specific perturbation, i.e., a force impulse on the wing’s CoM at mid-downstroke within a period of $0.1T$ with a magnitude of $150m_w$. Considering that the body flight dynamics is forced by the periodic aerodynamic loads due to the wing-flapping oscillations [51], the dynamic response of the flapping wing with flexible feathering hinge immediately after the external perturbations can be influenced interactively by the rotational and translational motions of the body at different forward flight speeds. In this study we keep the hawkmoth’s body locked to focus on the external disturbance-rejection robustness of the flexible wing hinge without consideration of the body vibration effects in all flight velocities. Further investigation on the vibrational stabilization mechanism in hawkmoth forward flight with flexible wing hinges will be explored in our future research. The flapping-wing dynamics under the impulse perturbation are expressed in Eq. (12) through the perturbation term, M_p . The timing of the force-impulse action in a wing-beat stroke is chosen at the mid-downstroke to achieve larger external perturbation torque, which has been examined additionally to barely affect the external disturbance-rejection robustness of the hawkmoth model. Therefore, the perturbation effects on vertical force production can be evaluated in terms of the normalized instantaneous vertical force [10], as defined by

$$C_{z,e}(t) = \frac{1}{T\bar{F}_z} \int_{t-0.5T}^{t+0.5T} F_{z,e} dt, \quad (16)$$

where \bar{F}_z is the cycle-averaged vertical force without perturbations and $F_{z,e}$ denotes the instantaneous vertical force after the perturbation. The dynamic response in terms of the vertical forces under vertical and horizontal perturbations are illustrated in Fig. 15 for various forward flight velocities.

As depicted in Fig. 15(a), the flapping wings with a flexible feathering hinge are perturbed under a vertical force impulse at the mid-downstroke of the third stroke cycle. At all flight velocities, the normalized instantaneous vertical force shows an immediate response to the perturbation, with a rapid drop at the end of the downstroke to approximately 82%–92% of the initial magnitude but achieving a quick recovery before the next wing beat starts. It takes less than two wing beats to restore the original and stable vertical force production. The dynamic response in terms of the wing kinematics due to the passive pitch rotation are further examined by investigating the time-varying feathering angles, which are plotted in Fig. 16. The feathering angles displays a shrink in amplitude right after the vertical perturbation for all flight velocities, with some pronounced variations in high angles of attack, which are responsible for enhancing the vertical force production against the large downward force impulse.

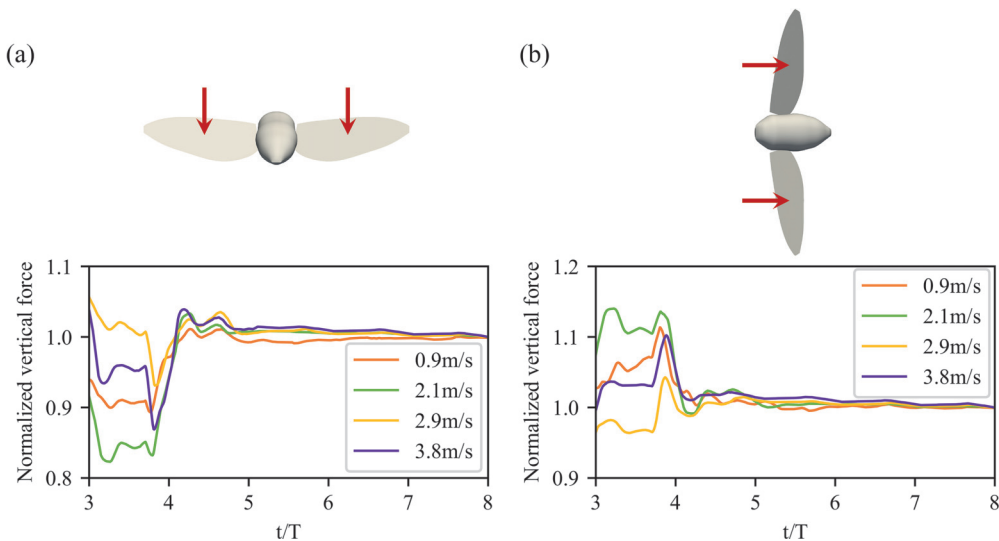


FIG. 15. Dynamic response of hawkmoth forward flight with flexible feathering hinge under force-impulse perturbation at various flight velocities. (a) Vertical perturbation. (b) Horizontal perturbation. The force impulse acts on the wing at mid-downstroke within a period of $0.17T$; the vertical force is normalized by the cycle-averaged vertical force without perturbations.

The dynamic response of flapping wings under a horizontal force impulse was also investigated. As shown in Fig. 15(b), the vertical forces rise by up to 14% immediately after the horizontal perturbation but recover in less than two wing beats to the original state at all flight velocities. The dynamic response of the wing kinematics shows a pronounced discrepancy in the feathering angle variations (Fig. 17) compared with the case of a vertical impulse (Fig. 16). This is manifested as a slight increase in the feathering amplitude at lower angles of attack, which can be inferred to reduce the fluid drag against the backward impulse.

There is also a noticeable discrepancy in the perturbation-induced dynamic response feature (Figs. 15–17) among the different forward flight velocities. The external disturbance rejection at a forward velocity of 2.9 m/s apparently outperforms the others in terms of the fluctuations in vertical force and restoration time. The impulse-induced fluctuation in the normalized instantaneous vertical force $C_{z,e}$ is less than 5% of the cycle-averaged vertical force without perturbations, \bar{F}_z (Fig. 15). This indicates that the external disturbance-rejection robustness is enhanced at intermediate forward flight velocities.

Based on our analysis and discussion of the effects of feathering-spring stiffness on flapping aerodynamic robustness at several flight velocities (Figs. 13 and 14), we found that while the wing-hinge stiffness plays a crucial role in altering the feathering amplitude, vertical force, power, and efficiency in all flight velocities, the realistic one is capable of achieving optimal aerodynamic force production while obtaining high power efficiency. Therefore, in this study to focus on the external disturbance-rejection robustness, we did not carry out an extensive study on the effects of feathering-spring stiffness on external disturbance-rejection robustness at several flight velocities, which will be discussed in our future research.

In summary, at various forward flight velocities, the hawkmoth model with flexible wing hinge demonstrates a remarkable external disturbance-rejection robustness to both vertical and horizontal perturbations. The flexible wing-hinge dynamic model with realistic feathering-spring stiffness enables a full recovery in aerodynamic force and wing kinematics within one to two wing beats, achieving stable and robust forward flight under various external disturbances.

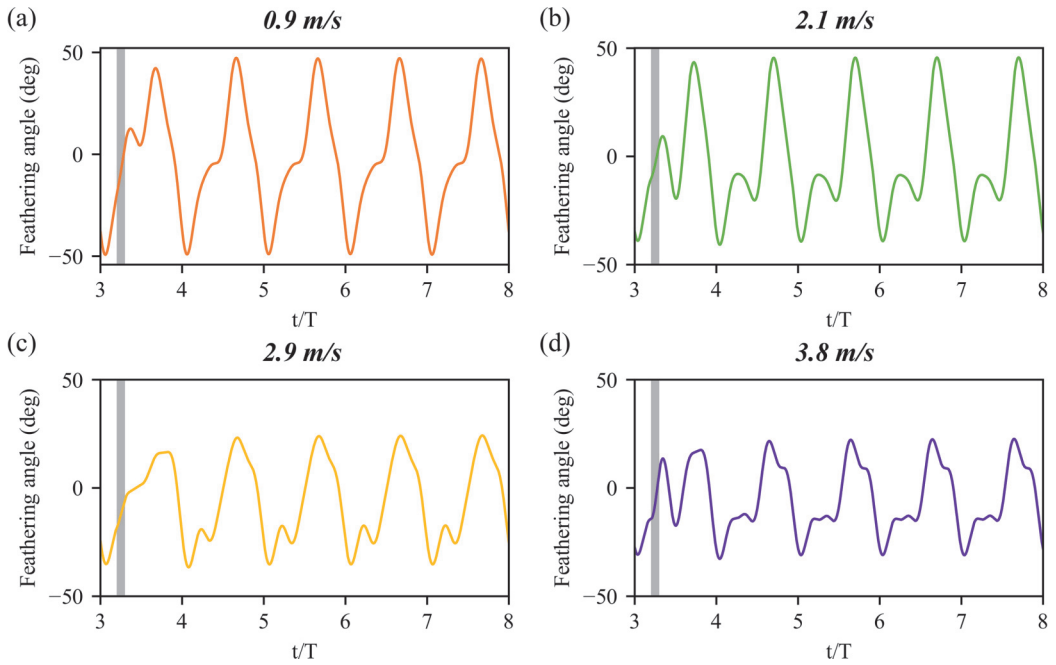


FIG. 16. Feathering angle variation under a vertical force-impulse perturbation at various flight velocities. (a) 0.9 m/s; (b) 2.1 m/s; (c) 2.9 m/s; (d) 3.8 m/s. Gray lines represent the duration of the impulse action.

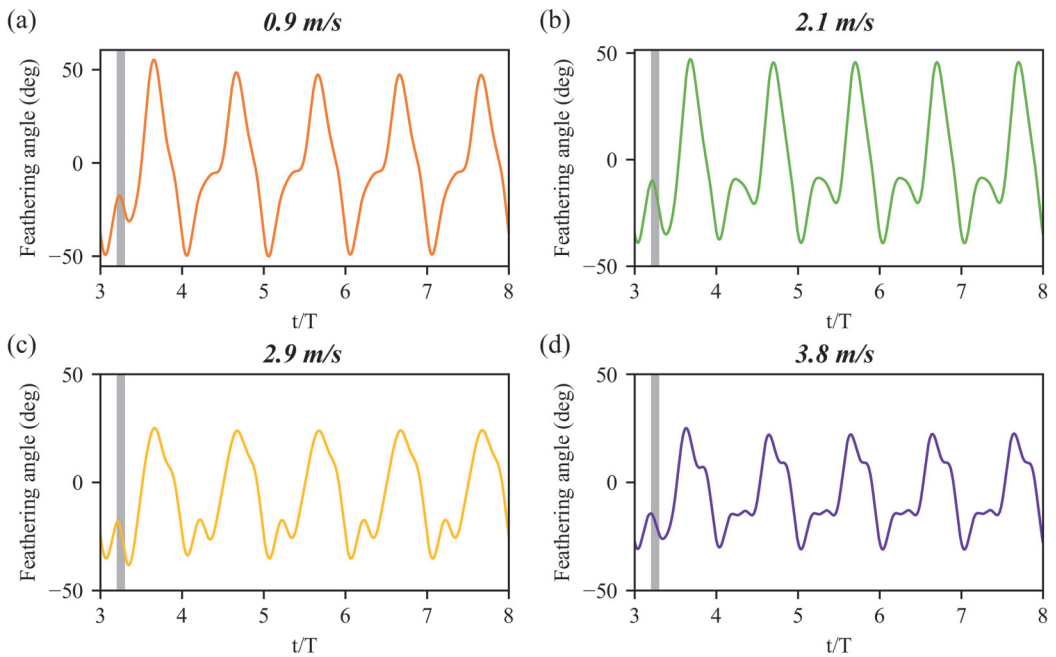


FIG. 17. Feathering angle variation under a horizontal force-impulse perturbation at various flight velocities. (a) 0.9 m/s; (b) 2.1 m/s; (c) 2.9 m/s; (d) 3.8 m/s. Gray lines represent the duration of the impulse action.

V. CONCLUDING REMARKS

This work addresses a simulation-based study of the aerodynamics and flight stability of the hawkmoth, *Manduca sexta*, with flexible wing hinge over a broad range of forward flight velocities. A FSI model that couples one-torsional-spring-based elastic wing-hinge dynamics and flapping aerodynamics has been utilized to explore the flow structures, aerodynamic force production, and power consumption associated with the flexible wing hinge at various flight velocities.

We have verified that the flexible wing hinge is capable of strengthening the LEV and BV, as well as their inherent interactions, and is hence responsible for augmenting the aerodynamic force production at all flight velocities, particularly by up to 6.5% of vertical force at fast flight speeds. The elastic-energy storage exhibits a J-shaped curve with increasing flight velocity, achieving remarkable energy-saving and high power efficiency at intermediate forward flight velocities. In addition, the flapping aerodynamic robustness was examined in terms of the feathering-spring stiffness dependency at five different stiffnesses over two orders of magnitude, indicating that the flexible wing-hinge-induced passive pitch rotation is robust at all flight velocities, while the realistic wing-hinge stiffness enables optimal aerodynamic force production and achieves high power efficiency. The realistic feathering-spring stiffness further shows remarkable external disturbance-rejection robustness when subjected to vertical and horizontal perturbations, enabling rapid and robust recovery in aerodynamic force production within one to two wing beats under various external disturbances.

Our study highlights the importance and significance of the flexible wing hinge in biomimetic designs for flapping micro aerial vehicles. The natural solution of hinge stiffness can serve as an engineering alternative to achieve optimal aerodynamic and stability performance for flapping micro aerial vehicles. This study has only focused on passive feathering with a one-torsional-spring-based elastic wing hinge, leaving more comprehensive analysis on the combination of an active stroke with a passive wing pitch and deviation using a three-torsional-spring-based elastic wing-hinge model for future research.

ACKNOWLEDGMENTS

This work was partly supported by JSPS KAKENHI Grants No. 19H02060 and No. 23H01373.

-
- [1] H. Liu, S. Wang, and T. Liu, Vortices and forces in biological flight: Insects, birds, and bats, *Annu. Rev. Fluid Mech.* **56**, 147 (2024).
 - [2] H. Liu, Simulation-based insect-inspired flight systems, *Curr. Opin. Insect Sci.* **42**, 105 (2020).
 - [3] W. Shyy, H. Aono, S. K. Chimakurthi, P. Trizila, C. K. Kang, C. E. S. Cesnik, and H. Liu, Recent progress in flapping wing aerodynamics and aeroelasticity, *Prog. Aerospace Sci.* **46**, 284 (2010).
 - [4] R. J. Bomphrey, Advances in animal flight aerodynamics through flow measurement, *Evol. Biol.* **39**, 1 (2012).
 - [5] T. Nakata and H. Liu, A fluid-structure interaction model of insect flight with flexible wings, *J. Comput. Phys.* **231**, 1822 (2012).
 - [6] T. T. Nguyen, D. S. Sundar, K. S. Yeo, and T. T. Lim, Modeling and analysis of insect-like flexible wings at low Reynolds number, *J. Fluids Struct.* **62**, 294 (2016).
 - [7] T. Deora, N. Gundiah, and S. P. Sane, Mechanics of the thorax in flies, *J. Exp. Biol.* **220**, 1382 (2017).
 - [8] T. Lindsay, A. Sustar, and M. Dickinson, The function and organization of the motor system controlling flight maneuvers in flies, *Curr. Biol.* **27**, 345 (2017).
 - [9] A. J. Bergou, L. Ristroph, J. Guckenheimer, I. Cohen, and Z. J. Wang, Fruit flies modulate passive wing pitching to generate in-flight turns, *Phys. Rev. Lett.* **104**, 148101 (2010).

- [10] X. Cai, Y. Xue, D. Kolomenskiy, R. Xu, and H. Liu, Elastic storage enables robustness of flapping wing dynamics, *Bioinspiration Biomimetics* **17**, 045003 (2022).
- [11] R. B. Srygley and A. L. R. Thomas, Unconventional lift-generating mechanisms in free-flying butterflies, *Nature (London)* **420**, 660 (2002).
- [12] A. L. R. Thomas, G. K. Taylor, R. B. Srygley, R. L. Nudds, and R. J. Bomphrey, Dragonfly flight: Free-flight and tethered flow visualizations reveal a diverse array of unsteady lift-generating mechanisms, controlled primarily via angle of attack, *J. Exp. Biol.* **207**, 4299 (2004).
- [13] R. J. Bomphrey, N. J. Lawson, N. J. Harding, G. K. Taylor, and A. L. R. Thomas, The aerodynamic of *Manduca sexta*: Digital particle image velocimetry analysis of the leading-edge vortex, *J. Exp. Biol.* **208**, 1079 (2005).
- [14] H. Wan, H. Dong, and K. Gai, Computational investigation of cicada aerodynamics in forward flight, *J. R. Soc. Interface* **12**, 20141116 (2015).
- [15] G. Liu, H. Dong, and C. Li, Vortex dynamics and new lift enhancement mechanism of wing-body interaction in insect forward flight, *J. Fluid Mech.* **795**, 634 (2016).
- [16] J. Song, B. W. Tobalske, D. R. Powers, T. L. Hedrick, and H. Luo, Three-dimensional simulation for fast forward flight of a calliope hummingbird, *R. Soc. Open Sci.* **3**, 160230 (2016).
- [17] J. Yao and K. S. Yeo, Forward flight and sideslip manoeuvre of a model hawkmoth, *J. Fluid Mech.* **896**, A22 (2020).
- [18] Y. Yao and K. S. Yeo, Longitudinal free flight of a model insect flyer at low Reynolds number, *Comput. Fluids* **162**, 72 (2018).
- [19] J. Wang, Y. Ren, C. Li, and H. Dong, Computational investigation of wing-body interaction and its lift enhancement effect in hummingbird forward flight, *Bioinspir. Biomim.* **14**, 046010 (2019).
- [20] H. Aono, F. Liang, and H. Liu, Near- and far-field aerodynamics in insect hovering flight: An integrated computational study, *J. Exp. Biol.* **211**, 239 (2008).
- [21] B. Liang and M. Sun, Aerodynamic interactions between wing and body of a model insect in forward flight and maneuvers, *J. Bionic Eng.* **10**, 19 (2013).
- [22] B. Liang and M. Sun, Aerodynamic interactions between contralateral wings and between wings and body of a model insect at hovering and small speed motions, *Chin. J. Aeronaut.* **24**, 396 (2011).
- [23] Y. Xue, X. Cai, and H. Liu, Effects of wing-body interaction on hawk moth aerodynamics and energetics at various flight velocities, *Phys. Fluids* **34**, 051915 (2022).
- [24] D. Ishihara, T. Horie, and M. Denda, A two-dimensional computational study on fluid-structure interaction cause of wing pitch changes in dipteran flapping flight, *J. Exp. Biol.* **212**, 1 (2009).
- [25] M. H. Dickinson, F. O. Lehmann, and S. P. Sane, Wing rotation and the aerodynamic basis of insect flight, *Science* **284**, 1954 (1999).
- [26] T. Beatus and I. Cohen, Wing-pitch modulation in maneuvering fruit flies is explained by an interplay between aerodynamics and a torsional spring, *Phys. Rev. E* **92**, 022712 (2015).
- [27] D. Kolomenskiy, S. Ravi, R. Xu, K. Ueyama, T. Jakobi, T. Engels, T. Nakata, J. Sesterhenn, K. Schneider, R. Onishi, and H. Liu, The dynamics of passive feathering rotation in hovering flight of bumblebees, *J. Fluids Struct.* **91**, 102628 (2019).
- [28] D. Ishihara, Role of fluid-structure interaction in generating the characteristic tip path of a flapping flexible wing, *Phys. Rev. E* **98**, 032411 (2018).
- [29] D. Ishihara, Computational approach for the fluid-structure interaction design of insect inspired micro flapping wings, *Fluids* **7**, 26 (2022).
- [30] H. Liu, S. Ravi, D. Kolomenskiy, and H. Tanaka, Biomechanics and biomimetics in insect-inspired flight systems, *Philos. Trans. R. Soc. B* **371**, 20150390 (2016).
- [31] A. P. Willmott and C. P. Ellington, The mechanics of flight in the hawkmoth *Manduca sexta*. I. Kinematics of hovering and forward flight, *J. Exp. Biol.* **200**, 2705 (1997).
- [32] A. P. Willmott and C. P. Ellington, The mechanics of flight in the hawkmoth *Manduca sexta*. II. Aerodynamic consequences of kinematic and morphological variation, *J. Exp. Biol.* **200**, 2723 (1997).
- [33] H. Liu and K. Kawachi, A numerical study of insect flight, *J. Comput. Phys.* **146**, 124 (1998).
- [34] H. Liu, C. P. Ellington, K. Kawachi, C. Van Den Berg, and A. P. Willmott, A computational fluid dynamic study of hawkmoth hovering, *J. Exp. Biol.* **201**, 461 (1998).

- [35] H. Liu, Integrated modelling of insect flight: From morphology, kinematics to aerodynamics, *J. Comput. Phys.* **228**, 439 (2009).
- [36] H. Liu and H. Aono, Size effects on insect hovering aerodynamics: An integrated computational study, *Bioinspir. Biomim.* **4**, 015002 (2009).
- [37] X. Zhang and H. Liu, A three-axis PD control model for bumblebee hovering stabilization, *J. Bionic Eng.* **15**, 494 (2018).
- [38] R. Xu, X. Zhang, and H. Liu, Effects of wing-to-body mass ratio on insect flapping flights, *Phys. Fluids* **33**, 021902 (2021).
- [39] X. Cai, D. Kolomenskiy, T. Nakata, and H. Liu, A CFD data-driven aerodynamic model for fast and precise prediction of flapping aerodynamics in various flight velocities, *J. Fluid Mech.* **915**, A114 (2021).
- [40] W. Shyy, H. Aono, C. Kang, and H. Liu, *An Introduction to Flapping Wing Aerodynamics* (Cambridge University Press, New York, 2013).
- [41] T. Nakata, H. Liu, and R. J. Bomphrey, A CFD-informed quasi-steady model of flapping-wing aerodynamics, *J. Fluid Mech.* **783**, 323 (2015).
- [42] R. J. Wood, The first takeoff of a biologically inspired at-scale robotic insect, *IEEE Trans. Rob.* **24**, 341 (2008).
- [43] S. A. Combes and T. L. Daniel, Flexural stiffness in insect wings I. Scaling and the influence of wing venation, *J. Exp. Biol.* **206**, 2979 (2003).
- [44] R. J. Wootton, Leading edge section and asymmetric twisting in the wings of flying butterflies (Insecta, Papilionoidea), *J. Exp. Biol.* **180**, 105 (1993).
- [45] J. C. R. Hunt, A. A. Wray, and P. Moin, Eddies, stream, and convergence zones in turbulent flows, Center for TURBULENCE research report CTR-S88, 193 (1988).
- [46] A. P. Willmott, C. P. Ellington, and A. L. R. Thomas, Flow visualization and unsteady aerodynamics in the flight of the hawkmoth, *Manduca sexta*, *Philos. Trans. R. Soc. London, Ser. B* **352**, 303 (1997).
- [47] S. M. Walker, D. A. Schwyn, R. Mokso, M. Wicklein, T. Müller, M. Doube, M. Stampanoni, H. G. Krapp, and G. K. Taylor, In vivo time-resolved microtomography reveals the mechanics of the blowfly flight motor, *PLoS Biol.* **12**, e1001823 (2014).
- [48] M. H. Dickinson and M. S. Tu, The function of dipteran flight muscle, *Comp. Biochem. Physiol., Part A: Mol. Integr. Physiol.* **116**, 223 (1997).
- [49] F. O. Lehmann, S. Gorb, N. Nasir, and P. Schützner, Elastic deformation and energy loss of flapping fly wings, *J. Exp. Biol.* **214**, 2949 (2011).
- [50] Z. Liu, X. Yan, M. Qi, Y. Zhu, D. Huang, X. Zhang, and L. Lin, Design of flexible hinges in electromagnetically driven artificial flapping-wing insects for improved lift force, *J. Micromech. Microeng.* **29**, 015011 (2018).
- [51] H. E. Taha, M. Kiani, T. L. Hedrick, and J. S. M. Greeter, Vibrational control: A hidden stabilization mechanism in insect flight, *Sci. Rob.* **5**, eabb1502 (2020).